Research in Nondestructive Evaluation

ISSN: 0934-9847 (Print) 1432-2110 (Online) Journal homepage: http://www.tandfonline.com/loi/urnd20

Quantitative Assessment of CFRP-concrete Cylinders Using Synthetic Aperture Radar Images

Tzuyang Yu

To cite this article: Tzuyang Yu (2017) Quantitative Assessment of CFRP-concrete Cylinders Using Synthetic Aperture Radar Images, Research in Nondestructive Evaluation, 28:3, 168-185, DOI: 10.1080/09349847.2016.1173266

To link to this article: http://dx.doi.org/10.1080/09349847.2016.1173266

Accepted author version posted online: 22 Apr 2016.
Published online: 22 Apr 2016.

RESEARCH IN NONDESTRUCTIVE EVALUATION
2017, VOL. 28, NO. 3, 168–185
http://dx.doi.org/10.1080/09349847.2016.1173266

Taylor & Francis
Taylor & Francis Group

Quantitative Assessment of CFRP-concrete Cylinders Using Synthetic Aperture Radar Images

Tzuyang Yu

Department of Civil and Environmental Engineering, University of Massachusetts Lowell, Lowell, Massachusetts, USA

ABSTRACT

A feature extraction algorithm is proposed to quantitatively assess the condition of intact and damaged carbon fiber reinforced polymer (CFRP)-wrapped concrete cylinders using synthetic aperture radar (SAR) images. The proposed algorithm converts SAR images into a simplified representation, based on the shape, size, and amplitude of SAR images. In this approach, the shape of scatterers in a SAR image is characterized by average Gaussian curvature (K), area ratio (R), and SAR amplitude (I), and is represented by a K-R-I curve. SAR images of intact and damaged CFRP-wrapped concrete cylinders were generated by a stripmap SAR imaging radar system (10.5 GHz) at various inspection angles (0°, 15°, 25°, 30°, 45°, and 60°). From our experimental result, it is found that the K-R-I representation of SAR images is capable of distinguishing damaged SAR images from intact ones at different inspection angles. Quantitative dissimilarity between the K-R-I curves of intact and damaged specimens is assessed by coefficient of correlation and compared with the signal-to-noise ratio (SNR) of SAR images. It is found that the dissimilarity of K-R-I curves is closely related to the SNR of SAR images, demonstrating the feasibility and potential of the proposed K-R-I representation.

KEYWORDS

CFRP-concrete; damage detection; radar NDE; synthetic aperture radar

1. Introduction

In the remote sensing of concrete structures for condition assessment, radar and microwave sensors are powerful tools to inspect surface and subsurface damages, among other sensors such as LiDAR and thermal infrared. When using radar and microwave sensors, synthetic aperture radar (SAR) imaging algorithms can be used to improve the resolution of radar images for better detection, characterization, and diagnosis. Integrated radar signals rendered in the SAR image domain can be used for target detection (e.g., range, size, damage), change detection [1], feature extraction [2,3], as well as damage detection [4,5]. Most remote sensing applications used cross-range–cross-range SAR images for surface inspection, while some applications used

CONTACT Tzuyang Yu tzuyang+yu@uml.edu Department of Civil and Environmental Engineering, University of Massachusetts Lowell, One University Avenue, Lowell, MA 01854, USA.

Color versions of one or more figures in the article can be found online at www.tandfonline.com/urnd.

range–cross-range SAR images for subsurface inspection [6,7]. In civil engineering, SAR imaging has also been applied in the subsurface damage (debonding) detection of fiber-reinforced polymer (FRP) wrapped/strengthened concrete structures to assess the quality of FRP repair/strengthening construction [6]. The capability of radar signals on penetrating through dielectrics (e.g., FRP, concrete) enables imaging radar to detect subsurface defects or to evaluate the aging of materials. As a result, studying the features of integrated scatterers in SAR images is key to the success of structural condition assessment using SAR imaging.

In general, subsurface damage detectability of reflected and scattered radar signals depends on the geometry (e.g., shape, surface roughness) and electromagnetic composition (e.g., property, distribution, contrast) of the target, radar frequency (wavelength), inspection range, incident angle, and inspection scheme (monostatic or bistatic). After integrating radar signals into SAR images, the scatterers in a SAR image represent the combined effect of all above-mentioned factors. Consequently, scatterers are used for condition assessment since they signal the presence of either a dielectric interface or change of geometry. Comparing two SAR images of intact and damaged structures facilitates damage detection and localization in such approach.

However, difficulties arise when performing direct comparison of SAR images. Direct comparison is usually carried out by background subtraction in order to remove background noise and to increase signal-to-noise ratio (SNR). In such scheme, an intact structure represents the background signal and a damaged structure represents both background and target signals. In order to correctly remove the background signal in a range–cross-range SAR image, perfect spatial alignment (both translation and rotation) of two images is required but very difficult to achieve in the field. Meanwhile, direct comparison of SAR images also utilizes only the amplitude information, which could be misleading for interpretation. This is because two SAR scatterers caused by intact and damaged structures may result in identical maximum amplitude but different shapes (distribution of amplitudes). As a result, quantitative analysis of SAR images for structural condition assessment requires delicate arrangement and is experience-oriented.

In view of the difficulties in the use of SAR imaging for structural condition assessment, our objective in this article is to present a simplified representation to quantify SAR images for damage detection. In this simplified representation, comparison of (range vs. cross–range) SAR images (matrices) is converted into the comparison of simplified K-R-I curves (vectors) generated from SAR images. Global measures including shape (K or Gaussian curvature), contour area ratio (R), and SAR amplitude (I) of each SAR image are computed for quantitative comparison.

In what follows, the theoretical basis of the proposed, simplified representation is first provided. Application of the simplified representation is made

on a CFRP-concrete cylinder that is inspected by a laboratory stripmap SAR imaging system. Finally, research findings are discussed and concluded.

2. Theoretical background

2.1. *Synthetic aperture radar imaging*

In synthetic aperture radar imaging, two formats are usually used for different applications; cross-range–cross-range (r_x-r_x) and range–cross-range (r-r_x). Figure 1 illustrates these two formats, using a cylinder as example. In Fig. 1, the representation of a cylinder in r_x-r_x images is a rectangle, while the one in r-r_x images is a circle. In this research, subsurface sensing is achieved by using range–cross-range (r-r_x) SAR images. Formation of range–cross-range (r-r_x) SAR images are briefly explained in this section.

Range–cross-range (r-r_x) SAR images are generated by backprojection algorithms [8]. Consider a stripmap SAR imaging mode shown in Fig. 2. At each radar location, an incident wave with unit amplitude is defined by [9]

$$\Psi_{inc}(\bar{r}) - \frac{1}{r}.\exp(i\bar{k}_i.\bar{r}) \tag{1}$$

where $\bar{k}_i = k_{ix}\,\hat{x} - k_{iy}\,\hat{y}$ is the incident wave vector and $\bar{r}$is the relative position vector from the radar to any observation point, $|\bar{r}| = r$. The scattered field from scatterer j at $\bar{r}_j$ and observed at $\bar{r}$is [10]:

$$\Psi_{scat}(\bar{r},\bar{r}_j) = \frac{S_j(\bar{r},\hat{k}_i)}{|\bar{r}-\bar{r}_j|}\exp(ik|\bar{r}-\bar{r}_j|).\Psi_{inc}(\bar{r}) \tag{2}$$

where $s_j = s_j(\bar{r},\hat{k}_i)$ is the scattered amplitude at scatterer j due to an incident wave at $\hat{k}_i$, observed at $\bar{r}$. By neglecting the interaction among scatterers, the total scattered field from N scatterers observed at $\bar{r}$is the summation of the scattered fields from all scatterers. Equation (3) is actually a sliced projection of the two-dimensional (2D) Fourier transform (FT) of the domain Ω_s:

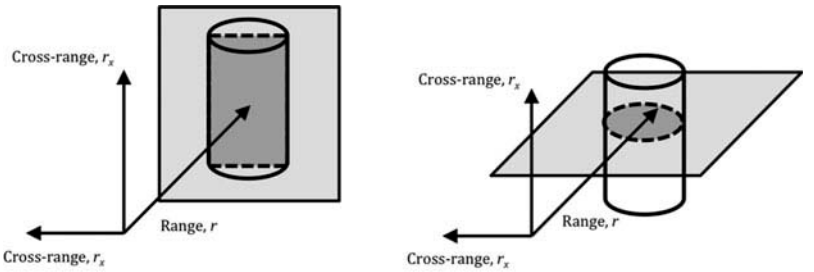

Figure 1. Two formats of SAR images.

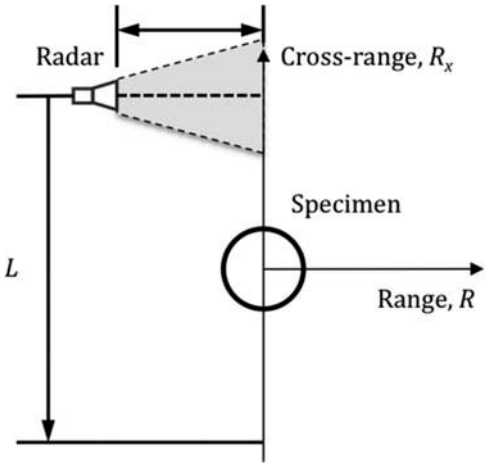

Figure 2. Stripmap SAR imaging mode.

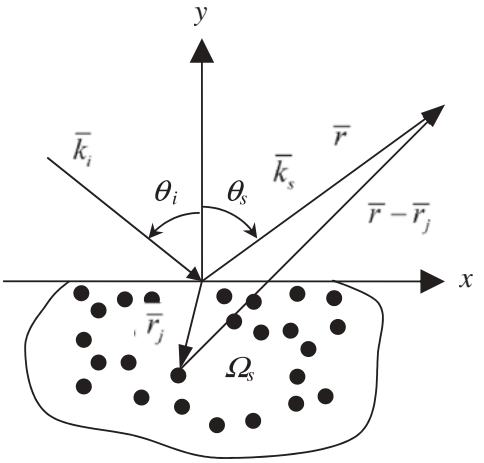

Figure 3. Scattering of N point scatterers.

$$\Psi_{scat}(\bar{r}) = \sum_{j=1}^{N} \frac{s_j(\bar{r}, \hat{k}_i)}{|\bar{r} - \bar{r}_j|} . \exp(ik|\bar{r} - \bar{r}_j|) . \Psi_{inc}(\bar{r}) \tag{3}$$

where $\bar{k}_s = k_{sx}\,\hat{x} + k_{sy}\,\hat{y}$ is the scattering direction vector $\bar{k}_s = -\bar{k}_i$ when the radar operates in monostatic mode. Figure 3 shows the scattering scheme in this formulation. Without losing generality, consider the case of single scatterer here. Knowing that $k = \omega/c$and $\theta = \theta_i = \tan^{-1}(k_{iy}/k_{ix})$, Eq. (2) can be written as

$$\Psi_{scat}(\omega, \theta) = \Psi_{scat}(k, \bar{r}_s) = \frac{s_\theta}{r^2} . \exp\left[i\frac{r}{c}\omega(1 + \cos^2\theta - \sin^2\theta\right]. \tag{4}$$

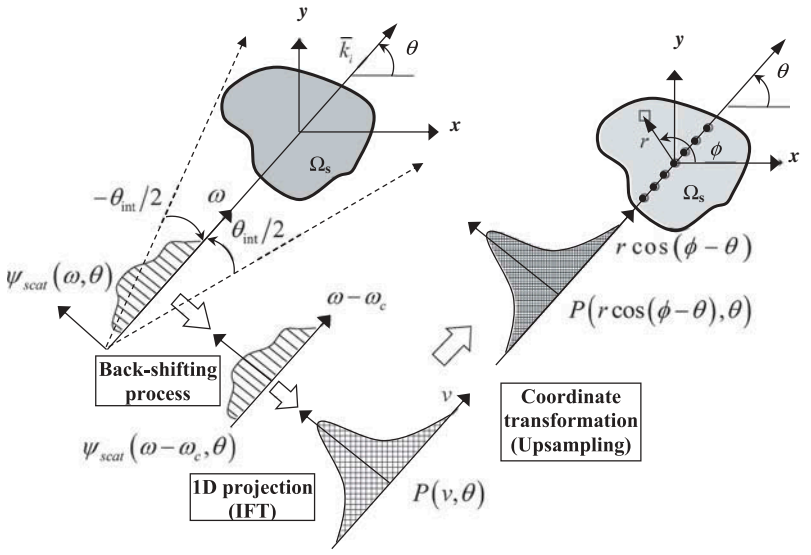

Figure 4. Conceptual description of backprojection algorithms [6].

In backprojection algorithms, one-dimensional (1D) inverse FT (IFT, line projection) is first performed to generate subimages. The final image is rendered by summing up all subimages. The center in backprojection images is coincided with the center of the scatterer by performing a modulation operation in frequency domain or a convolution operation in time domain. The shifting-back step in the backprojection algorithm in the frequency domain is performed by applying a ramp filter in which frequency ω_n is shifted back by a carrier frequency ω_c [11]. Scattering response in subimages can be described as

$$P(v,\theta) = \int_{\omega_{\min}}^{\omega_{\max}} d\omega \cdot \psi_{scat}(\omega-\omega_c,\theta)|\omega-\omega_c| \cdot \exp(-i\omega v) \tag{5}$$

$$= \frac{S_\theta}{r^2} \cdot \int_{\omega_{\max}}^{\omega_{\min}} d\omega . |\omega-\omega_c| . \exp\left[i\frac{r}{c}(\omega-\omega_c)(1+cos^2\theta-\sin^2\theta)-i\omega v\right] \tag{6}$$

where v is the spatial variable of the 1D IFT projection. Translating the local 1D IFT coordinate $(v, P(v,\theta_s))$to the global polar coordinate (r,ϕ)indicates that

$$v = r\cos(\phi-\theta_s). \tag{7}$$

Transforming from $P(v,\theta)$to $P(r\,cos(\phi-\theta),\theta)$is usually associated with upsampling in order to improve image quality. In other words, $P(r\,cos(\phi-\theta),\theta)$is the interpolated version of $P(v,\theta)$. The final backprojection (range–cross-range) image is obtained by integrating the subimages along the entire synthetic aperture:

$$I(r,\phi) = \int_{-\theta_{\text{int}}/2}^{\theta_{\text{int}}/2} d\theta \cdot P(r\cos(\phi-\theta),\theta). \tag{8}$$

This process can be conceptually illustrated by Fig. 4. Equation (8) can be converted into its Cartesian form as

$$x = r\cos\phi \tag{9}$$

$$y = r\sin\phi \tag{10}$$

such that range–cross-range images can be obtained as long as the orientation of synthetic aperture is specified. Computational issues related to image interpolation can be found in the texts on SAR [12,13]. Major advantages of backprojection algorithms include: (1) lower and localized artifact levels than frequency-domain algorithms, (2) easy adjustment to an approximate inverse formula for perturbed problems, (3) readily for parallel computing with limited interprocessor communications, and (4) simple motion compensation by time-shift operation [14,15].

2.2. *Simplified representation of radar images*

In this article, a simplified representation is proposed to convert range-cross-range SAR images ($I(r, r_x)$) into three-dimensional (3D) curves for quantitative analysis. This conversion is performed by calculating the following properties of SAR images:

$$K_{avg}(I_i) = \frac{1}{n}\sum_{i=1}^{n} K_i(x,y) = \frac{1}{n}\sum_{i=1}^{n}\left[\frac{\frac{\partial^2 I_i}{\partial x^2}\frac{\partial^2 I_i}{\partial y^2} - \left(\frac{\partial^2 I_i}{\partial x \partial y}\right)^2}{1+\left(\frac{\partial I_i}{\partial x}\right)^2 + \left(\frac{\partial I_i}{\partial y}\right)^2}\right] \tag{11}$$

$$R_A(I_i) = \frac{A(I_i)}{A_{\max}} \tag{12}$$

where $K_{avg}(I_i)$ = average Gaussian curvature [16] at a given SAR amplitude I_i, $R_A(I_i)$ = area ratio at a given SAR amplitude I_i, $A_{\max}$ = maximum closed area of the scatterer. The reason for calculating these two parameters is mainly to quantify the scattering phenomenon of radar signals (electromagnetic waves) in SAR images. When a point target is imaged by SAR, its scattering pattern will be circular (or circular scatter). When a rectangular target is imaged by SAR, its scattering pattern will be irregular, containing specular returns and edge reflections. If dielectric targets are encountered, multiple reflections from inside the target can be expected, making the scattering pattern even more complicated to interpret. In this article, average Gaussian curvature and area ratio, both at given SAR amplitudes, are calculated to quantify the change of scattering pattern in SAR images. Average Gaussian curvature is used to measure the distribution of SAR amplitudes in space, while area ratio

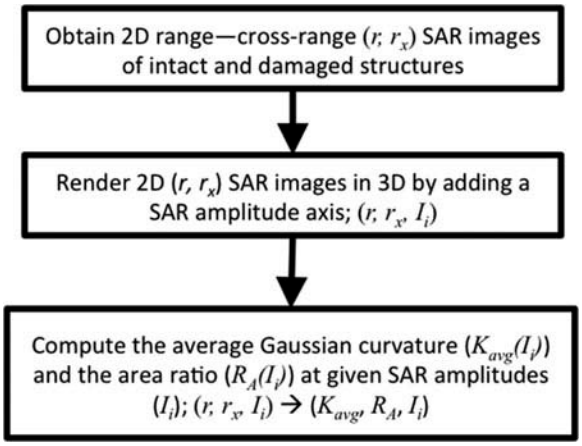

Figure 5. Procedure of the proposal simplified representation.

is used to measure the electromagnetic property of the target. The proposed representation is described by a procedure shown in Fig. 5. After applying the procedure, original SAR images is converted into (K_{avg}, R_A, I_i) curves.

3. Applications

3.1. *Artificial objects*

To demonstrate the feasibility of the proposed simplified (or K-R-I) representation, two artificial, simple 3D objects are considered: a cylinder and a cone. Figure 6 shows the 2D and 3D forms of an artificial, cylinder-type SAR image with its K-R-I curve. Figure 7 shows another example using an artificial, cone-type SAR image.

In Fig. 6, constant R_A and constant K_{avg} suggest a uniform amplitude distribution, while varying R_A and constant K_{avg} suggest a nonuniform amplitude distribution with consistent pattern (shape).

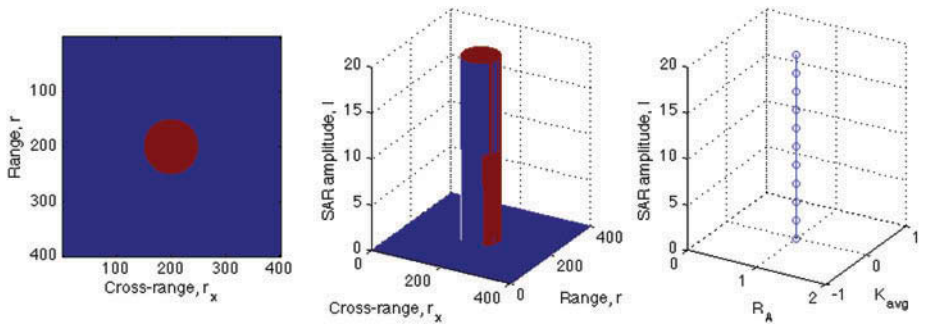

Figure 6. Application of the K-R-I representation using a cylinder as example.

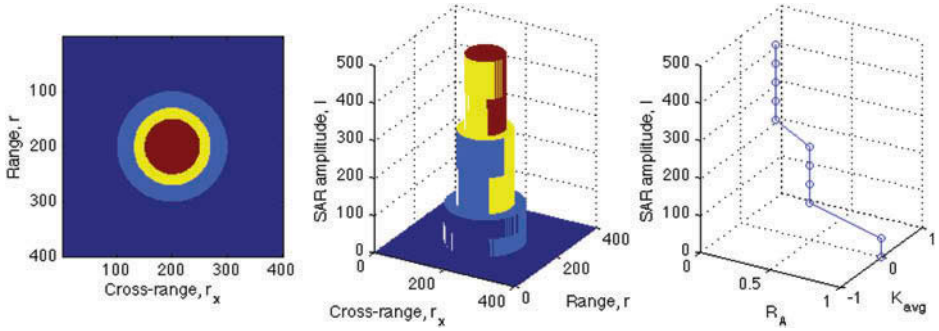

Figure 7. Application of the K-R-I representation using a cone as example.

3.2. *Steel plate*

A rectangular steel plate (40 cm x 60 cm x 2 cm) was used in generating real SAR images for testing the proposed representation algorithm. A laboratory 10.5 GHz central frequency imaging radar system with 4 GHz bandwidth was used to generate stripmap SAR images of the plate. Figure 8 shows a photograph of the plate and its SAR image. The physical configuration of the plate in Fig. 8(b) corresponds to the SAR image plane (range–cross-range) in Fig. 8(c). A 3D representation of the image is provided in Fig. 8(d). The contour line at a given SAR amplitude (I = 1,000) for calculating K_{avg} and R_A is shown in Fig. 8(e) as an example. After calculating the (K_{avg}, R_A) for different SAR amplitudes (I_i), the K-R-I curve of the SAR image is obtained as shown in Fig. 8(f). In Fig. 8, it is shown that amplitude change is continuous and the distribution of SAR amplitudes (shape of scatterer) is irregular in real SAR images. Note that the magnitude of K_{avg} values in this rectangular steel plate is in the range of [0, -0.02].

3.3. *CFRP-concrete cylinder*

An artificially damaged CFRP-wrapped concrete cylinder was used to examine the performance of proposed representation algorithm. A concrete cylinder specimen with a height of 30 cm and diameter of 15 cm was fabricated and wrapped with a CFRP layer. The FRP layer was adhered to the concrete cylinder by epoxy resin. A 5 cm x 5 cm x 0.5 cm artificial defect (made of Styrofoam) was embedded at the interface between the concrete and the FRP layer and targeted for subsurface defect detection. This defect size was chosen to verify the feasibility of both radar imaging (10.5 GHz, wavelength = 2.86 cm) and the proposed K-R-I representation. Different sizes of defect can be considered with the use of different radar frequencies. The water-to-cement ratio of concrete was 0.5, and the specimen was moist-cured for 28 days before the wrapping of an FRP layer. The side of the cylinder with a

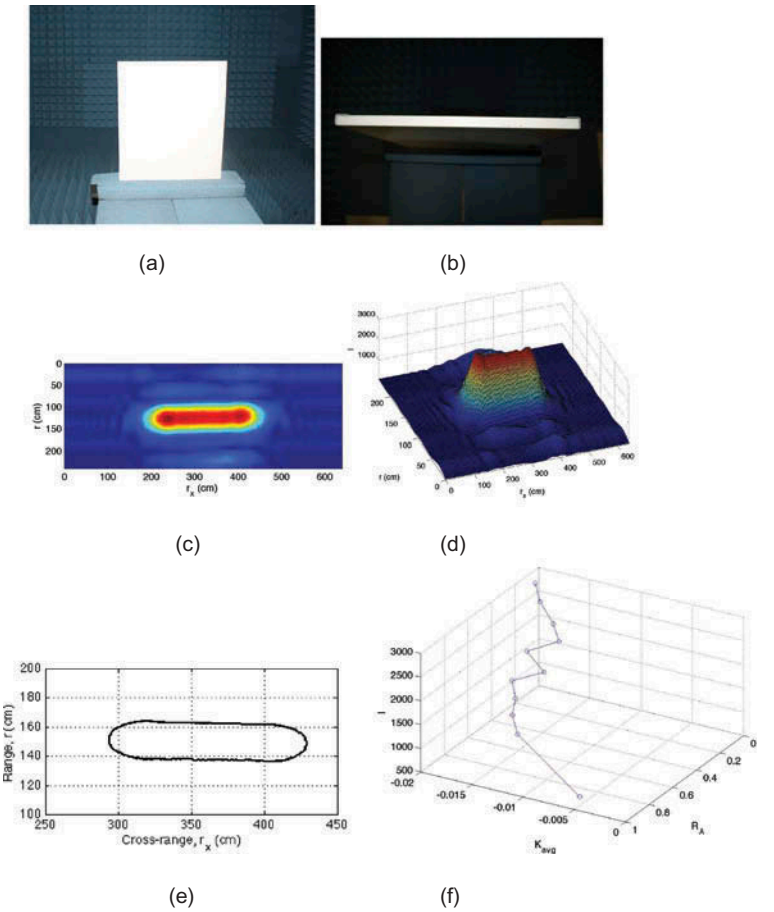

Figure 8. Rectangular steel plate: its SAR image and K-R-I curve. (a) Steel plate (front view); (b) steel plate (top view); (c) 2D SAR image; (d) 3D SAR image; (e) contour line at a given SAR amplitude (I=1,000); (f) K-R-I curve of the 3D SAR image.

subsurface defect is the damaged side, whilst the side without the defect is the intact side of the cylinder. Design of the CFRP-concrete cylinder is illustrated in Fig. 9.

Stripmap SAR imaging measurements at θ = [0, 15, 25, 30, 45, 60] degrees were carried out, and their K-R-I curves were generated as shown in Figs. 10–21. The reason for conducting SAR imaging at different angles is due to the angular dependence of target signals representing the presence of subsurface defect, as reported in literature [17].

Comparing Figs. 10 and 11, it is found that specular return dominates the intact response (Fig. 10) since the front surface of the FRP-concrete cylinder is perpendicular to the line of sight of radar at $\theta = 0$ degree. Compared to the SAR response of a steel plate in Fig. 8, it is also found that the SAR amplitudes in Fig. 10 are not distributed uniformly along the cross-range direction. This is because the surface of FRP overlay is unsmooth and rugged. On the other hand,

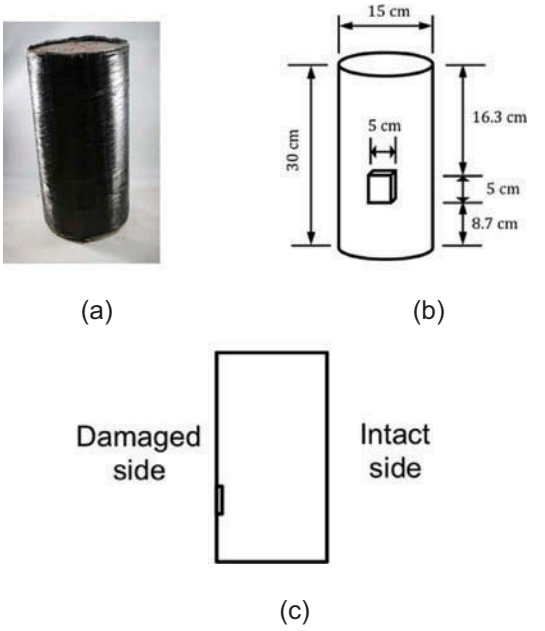

Figure 9. Design of an artificially damaged CFRP-concrete cylinder. (a) CFRP-concrete cylinder; (b) design of the cylinder; (c) damaged and intact sides.

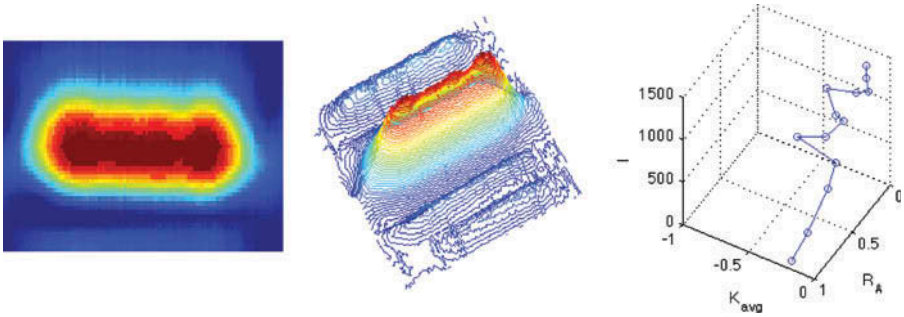

Figure 10. Stripmap SAR image and its K-R-I curve, intact side, θ = 0-deg.

in Fig. 11, SAR amplitude of the damaged side of FRP-concrete cylinder contains both the specular return from the front surface and the scattering signal due to a subsurface defect. As a result, some SAR amplitudes are reduced, and some are amplified. To account for the shape change (amplitude and its spatial distribution) in SAR images, the proposed representation was applied, and two distinctive K-R-I curves were obtained. Same image processing was applied to SAR images of intact and damaged sides of the CFRP-concrete cylinder at θ = 15, 25, 30, 45, 60 degrees, as shown in Figs. 12–21.

In Figs. 12–21, it is demonstrated that the SAR images of both intact and damaged sides of the CFRP-concrete specimen depend on inspection angle,

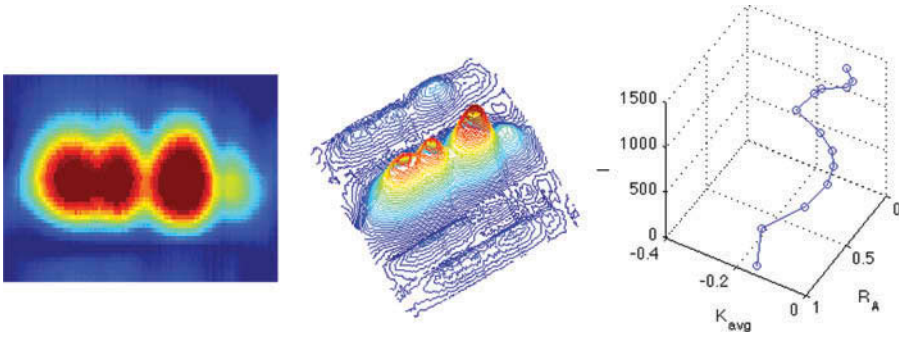

Figure 11. Stripmap SAR image and its K-R-I curve, damaged side, θ = 0-deg.

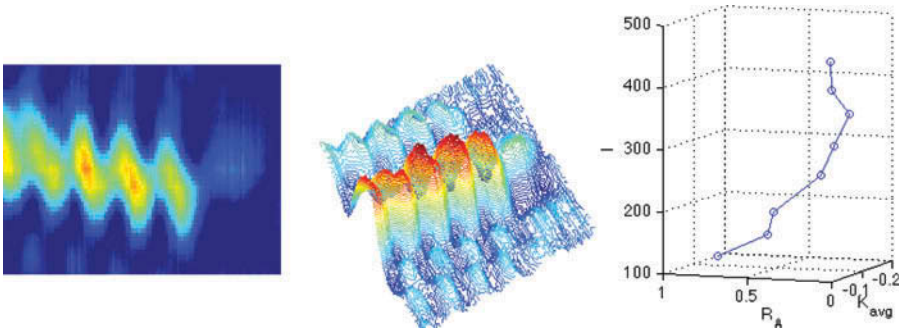

Figure 12. Stripmap SAR image and its K-R-I curve, intact side, θ = 15-deg.

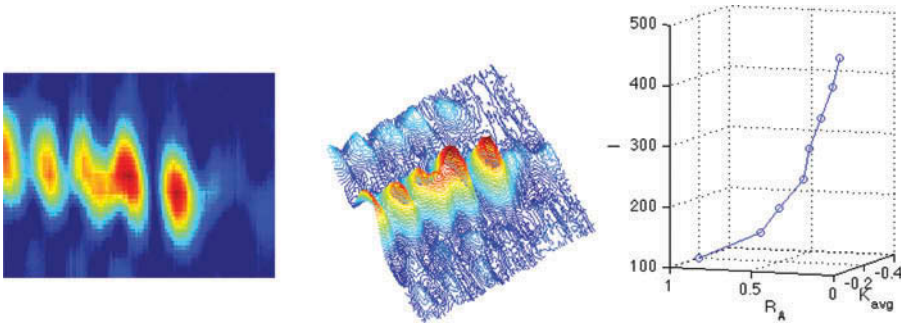

Figure 13. Stripmap SAR image and its K-R-I curve, damaged side, θ = 15-deg.

in terms of SAR amplitude and the distribution SAR amplitude. Such change is also reflected in the K-R-I representation of each SAR image.

3.4. *Validation of the proposed algorithm*

To validate the performance of the proposed K-R-I representation on condition assessment of structures, a forward study was conducted by comparing the coefficient of correlation between K-R-I curves with the signal-to-noise

ratio in the SAR images (SNR_I) of intact and damaged sides of a CFRP-concrete cylinder. The hypothesis was that the K-R-I curve of intact cylinder has a low coefficient of correlation with the one of damaged cylinder, suggesting the difference between an intact side SAR image from an damaged side SAR image. SNR_I was computed by comparing the SAR amplitude at the location of a known defect with the SAR amplitude at the location without a defect. It is defined by

$$SNR_I = \frac{I_{dam}}{I_{int}} \tag{13}$$

where I_{dam} = SAR amplitude at the location with a known defect (damaged), and I_{int} = SAR amplitude at the location without a defect (intact). Inspection angle was also considered in this validation since all SAR images (or K-R-I curves) are dependent on the selected inspection angle. Figure 22 describes the overview of this forward study.

SNR_I values defined by Eq. (13) were calculated in this forward study in which the location of a subsurface artificial defect was known. Computed SAR amplitudes for determining the SNR_I between intact and damaged SAR images are listed in Table 1, as well as the coefficients of correlation between intact and damaged K-R-I curves. These values are illustrated in Fig. 23. It is noteworthy to point out that only two K-R-I curves of identical length can be compared when computing their coefficient of correlation.

In Fig. 23, it is found that the SNR_I curve and the coefficients of correlation of K-R-I curves show an almost opposite trend. This is because, in the SNR_I approach, the higher the SNR_I value is, the more likely to indicate the presence of damage. On the other hand, in the K-R-I approach, the more dissimilarity (lower values of coefficient of correlation) between an intact K-R-I curve and an unknown K-R-I curve, the more likely to indicate the presence of damage. In other words, in the K-R-I approach, the lowest value of coefficient of correlation (highest dissimilarity between an intact K-R-I curve and an unknown K-R-I curve) suggests the presence of defect at an optimal inspection angle. This is validated by the opposite trends of the SNR_I and coefficient of correlation curves in Fig. 23.

4. Discussion

4.1. *Local versus global*

When using SAR images for damage localization, perfect alignment is needed in order to perform accurate background subtraction. This requires identical experimental setup for intact and damaged structures, which can be difficult to achieve in the field. If the SNR_I approach is adopted, a priori knowledge about possible damage locations must be provided in order to calculate the

SNR_I of each defect, as well as local SAR amplitudes are needed. It indicates that the SNR_I approach is a local method. Compared to traditional SAR imaging for damage detection using SNR_I, the proposed K-R-I representation does not need to know the location of a defect. Instead, it compares the shape and size distributions at various SAR amplitudes between intact and damaged structures. In other words, the proposed K-R-I representation is a global method.

4.2. *Effect of inspection angle*

In Figs. 8, 11, 14, 17, 20, and 23, shape and length of K-R-I curves vary in both intact and damaged sides of the FRP-concrete cylinder. This is due to the nature of stripmap SAR imaging using monostatic radar configuration. When the imaging radar captures the specular return of radar signals (θ = 0-deg.), strong background is likely to cover the scattering response of a defect (Figs. 6–8). When the monostatic imaging radar inspects a damaged structure at a steep angle (θ = 60-deg.), both the background and the defect signals are weakened and, consequently, their K-R-I curves are changed. In other words, K-R-I curves will change with the variation of inspection angle.

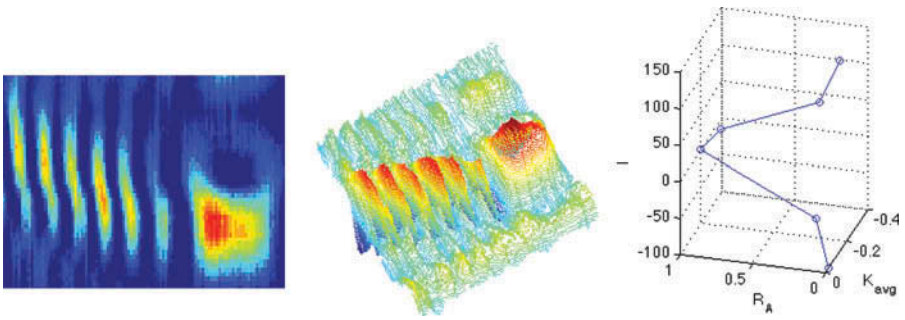

Figure 14. Stripmap SAR image and its K-R-I curve, intact side, θ = 25-deg.

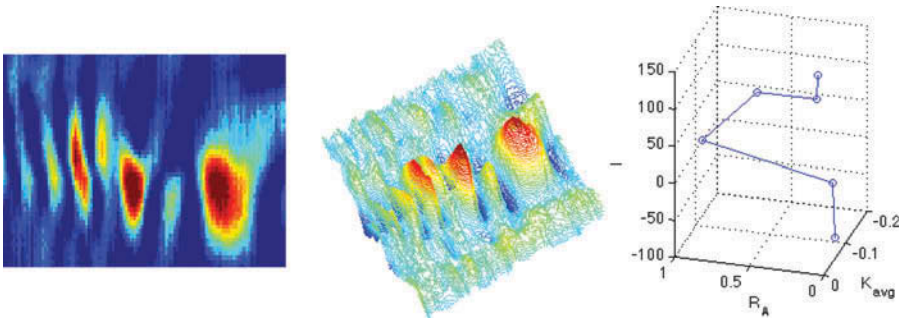

Figure 15. Stripmap SAR image and its K-R-I curve, damaged side, θ = 25-deg.

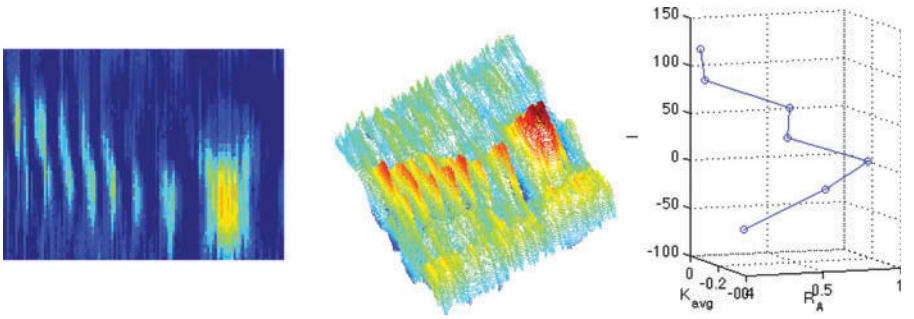

Figure 16. Stripmap SAR image and its K-R-I curve, intact side, θ = 30-deg.

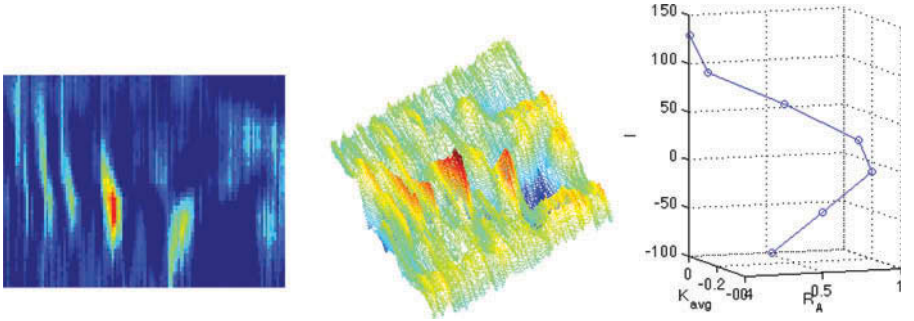

Figure 17. Stripmap SAR image and its K-R-I curve, damaged side, θ = 30-deg.

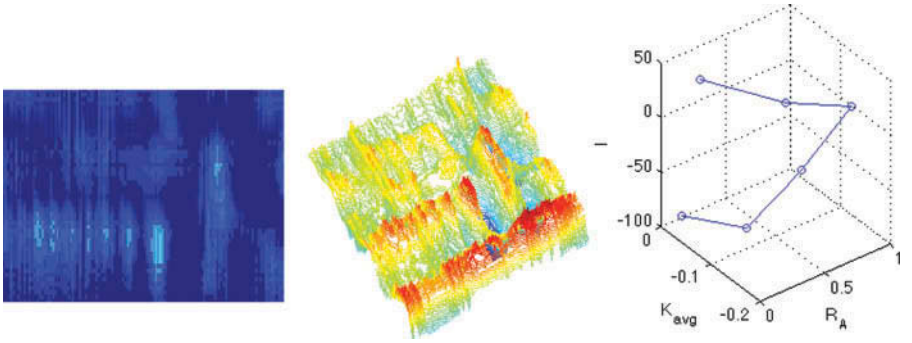

Figure 18. Stripmap SAR image and its K-R-I curve, intact side, θ = 45-deg.

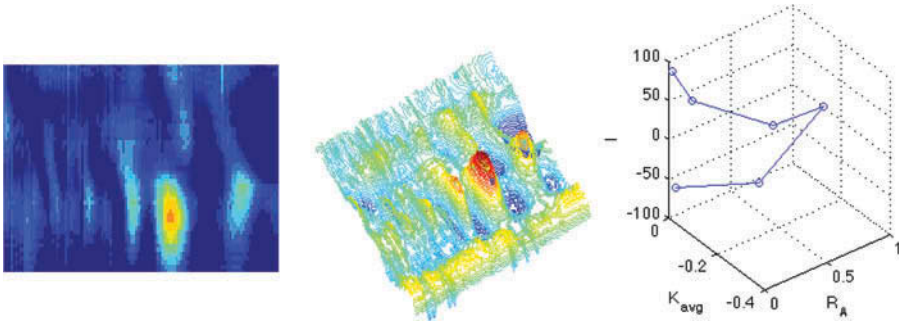

Figure 19. Stripmap SAR image and its K-R-I curve, damaged side, θ = 45-deg.

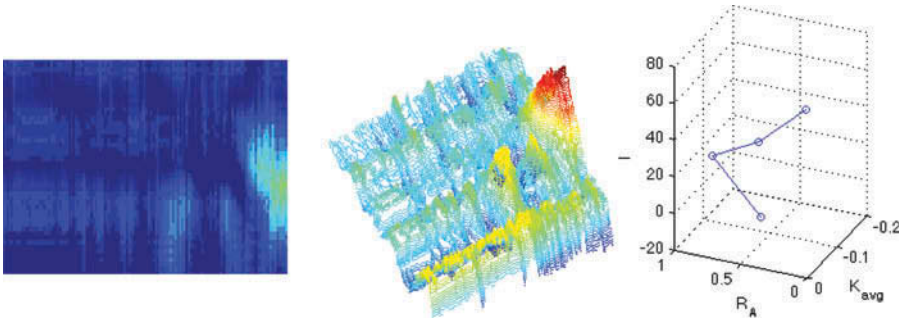

Figure 20. Stripmap SAR image and its K-R-I curve, intact side, θ = 60-deg.

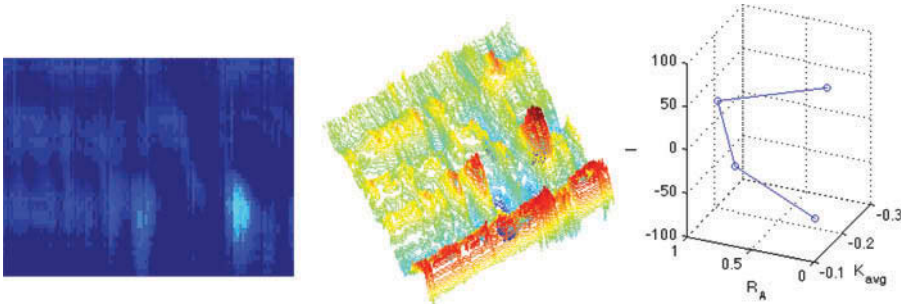

Figure 21. Stripmap SAR image and its K-R-I curve, damaged side, θ = 60-deg.

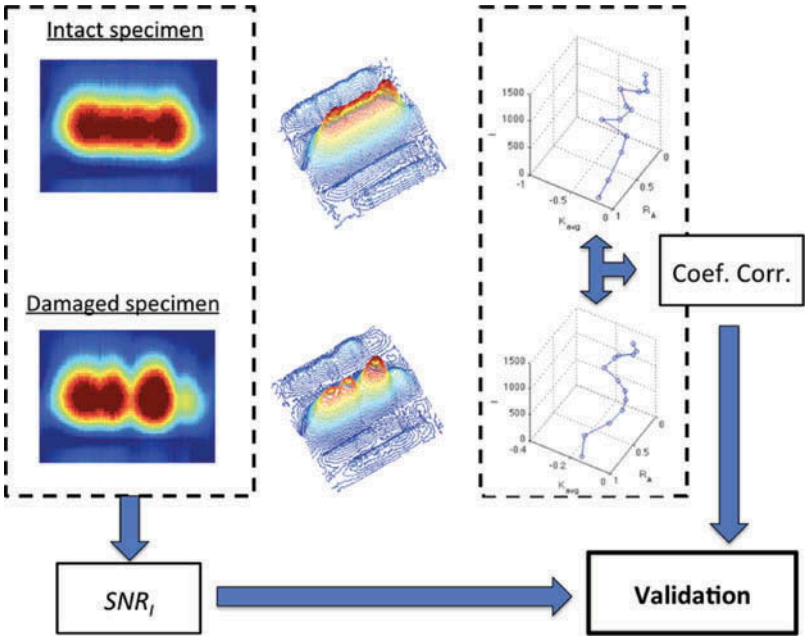

Figure 22. Schematic of a forward study for algorithm validation.

Table 1. Performance comparison between the K-R-I curves and the SNR_I of SAR images.

Inspection angle	Background (or noise) (I_{int})	Target signal (I_{dam})	SNR_I	Coef. corr.
0-deg.	913	1,209	0.7552	0.9571
15-deg.	643	499	1.2886	0.9923
25-deg.	230	110	2.0909	0.9854
30-deg.	165.9	70	2.3700	0.9487
45-deg.	110	20	5.5000	0.7045
60-deg.	40	10	4.0000	0.8164

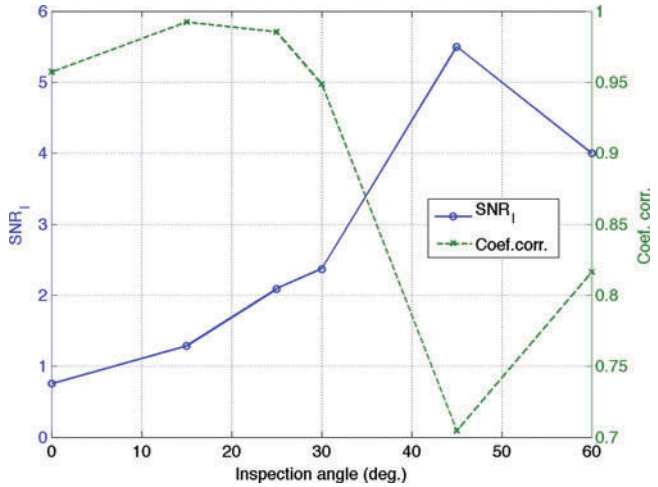

Figure 23. Comparison between traditional SNR approach and the K-R-I representation of SAR images.

4.3. *Limitations*

The proposed K-R-I representation has limitations when applied to real structures. First of all, it is a global approach and does not provide the location information of a defect. Although the K-R-I curves still preserve features of shape and size (relative) of SAR scatterers at different SAR amplitudes, generation of K-R-I curves from SAR images does not require the knowledge of coordinates (local or global). Therefore, K-R-I curves do not provide any spatial information for locating defects. Secondly, due to the use of relative area ratio, two SAR scatterers with identical shapes (amplitude distributions), but different sizes will lead to identical K-R-I curves. This is because that the concept of damage detectability in the proposed K-R-I approach is based on the coupled variation of shape and size at different SAR amplitudes. This limitation may be removed by using absolute areas instead of relative area ratios.

5. Conclusions

A simplified representation utilizing the shape (K_{avg}), size (R_A), and amplitude (I_i) of SAR images is proposed to extract the features in SAR images and to overcome

existing difficulties in quantitatively comparing SAR images for condition assessment. The proposed K-R-I representation is a global assessment of SAR images, based on the concept of shape-size coupling at different SAR amplitudes. From the application on a CFRP-concrete cylinder, it is demonstrated that the proposed K-R-I representation can differentiate intact SAR images from damaged SAR images. The performance of the K-R-I approach is also validated by traditional SNR approach. While this approach is limited by its global feature and unable to differentiate two same-shape-but-different-size SAR images, further research can be conducted to improve these properties.

Acknowledgment

The author would like to thank Prof. Ming L. Wang for hosting his visit in the Department of Civil and Environmental Engineering at Northeastern University during September–December 2015.

Funding

The authors want to acknowledge the financial support from the U.S. Department of Transportation (DOT) (Washington, D.C.) Office of Assistant Secretary for Research and Technology (OST-R) Commercial Remote Sensing and Spatial Information Program (CRS&SI) via a Phase VI project (Grant No. OASRTS-14-H-UML). The views, opinions, findings and conclusions reflected in this presentation are the responsibility of the authors only and do not represent the official policy or position of the USDOT/OST-R, or any State or other entity Reference.

References

[1] F. Bovolo and L. Bruzzone. *IEEE Transactions on Geoscience and Remote Sensing* **43**:2963–2972 (2005).
[2] M. Mazzolena. Tyrrhenian Workshop Advances in Radar and Remote Sensing (TyWRRS), pp.1 00–105, Sept. 12–14, 2012.
[3] C.O. Dumitru and M. Datcu. *IEEE Trans Geoscience and Remote Sensing* **51**(8):4591–4610 (2013).
[4] P. Uprety and F. Yamazaki. *IEEE Intl Geoscience and Remote Sensing Symposium (IGARSS)*, pp. 6829–6832, July 22–27, 2012.
[5] M. Sato, K. Takahashi, H. Liu, and C. Koyama. *IEEE Intl Geoscience and Remote Sensing Symposium (IGARSS)*, pp. 2601–2604, July 13–18, 2014.
[6] T. Yu. *ASCE Journal of Engineering Mechanics* **137**(8):547–560 (2011).
[7] C. Koyama, K. Takahashi, Y. Iitsuka, and M. Sato. *Asia-Pacific Microwave Conference (APMC)*, pp. 1025–1027, Nov. 4–7, 2014.
[8] A.C. Kak and M. Slaney. *Principles of Computed Tomographic Imaging*. Society of Industrial and Applied Mathematics (2001).
[9] J.A. Kong. *Electromagnetic Wave Theory*. EMW Publishing, Cambridge, MA (2000).
[10] L. Tseng, J.A. Kong, and K-H. Ding. *Scattering of Electromagnetic Waves, Theories and Applications*. Wiley, New York (2000).
[11] M.D. Desai and W.K. Jenkins. *IEEE Trans. on Image Processing*, pp. 505–512 (October 1992).

[12] W.G. Carrara, R.M. Majewski, and R.S. Goodman. *Spotlight Synthetic Aperture Radar: Signal Processing Algorithms*. Artech House, Boston, MA (1995).
[13] M. Soumekh. *Synthetic Aperture Radar Signal Processing with MATLAB Algorithms*. Wiley, New York (1999).
[14] J. McCorkle and M. Rofheart. *Proceedings of SPIE*. **2747**: 25–36 (1996).
[15] S. Nilsson and L.-E. Andersson. *Proceedings of SPIE*. **3370**: 62–72 (1998).
[16] E. Kreyszig. *Differential Geometry*. Dover, New York (1991).
[17] T. Yu and O. Buyukozturk. *NDT&E International* **41**:10–24 (2008).